A COLD AIR OUTBREAK NEAR SPITSBERGEN IN SPRINGTIME – BOUNDARY-LAYER MODIFICATION AND CLOUD DEVELOPMENT

BURGHARD BRÜMMER and BIRGIT RUMP

Meteorological Institute, University of Hamburg, Hamburg, Germany

and

GOTTFRIED KRUSPE

Max-Planck-Institute of Meteorology, Hamburg, Germany

(Received in final form 7 January, 1992)

Abstract. A moderate cold air outbreak from the Arctic ice over the warm West-Spitsbergen current on 15 and 16 May 1988 during the field experiment ARKTIS '88 is analysed using data from four aircraft and one research vessel.

The downstream development of cloud coverage appears to depend sensitively on the moisture content above the inversion. The cloud amount determines the energy balance at the sea surface. Under daytime conditions and little cloud cover, energy is added to the ocean in spite of sensible and latent heat losses.

The downstream temperature increase in the boundary layer is controlled by sensible heat flux and by longwave radiation cooling. The entrainment sensible heat flux is the dominating term in the region near the ice edge. The downstream moisture increase is controlled by surface evaporation. Condensation processes play no significant role.

On 16 May 1988 cloud streets near the ice edge changed to closed cloud meanders in the downstream direction. The aspect ratio increased from 3 to around 10 over a distance of 200 km. In the cloud street region, the dynamical generation of turbulent kinetic energy due to wind shear at the tilted inversion was larger than the thermal generation.

Cloud droplet concentration, mean droplet radius and liquid water content increased linearly with height. The maximum liquid water content was only 0.1 g/kg near the top of a 400 m thick closed cloud and clearly below the adiabatic value. The net longwave radiation flux decreased by 50 W/m^2 at cloud top and increased by 13 W/m^2 at cloud base.

1. Introduction

Outbreaks of cold air from the polar ice caps and in winter from the continents over adjacent warm oceans cause large sensible and latent heat transfers from the ocean to the atmosphere which can reach several 100 W/m^2 in extreme cases. Such weather episodes lead to the largest worldwide air–sea energy exchanges and contribute substantially to the total air–sea energy exchange in high and middle latitudes.

Preferred locations of cold air outbreaks are the Greenland Sea, Barents Sea and Bering Sea as well as the warm ocean currents on the east sides of the continents. Extensive cold air outbreaks typically cover areas of about 10^6 km^2 and can reach equatorward to below 30° lat to the rear of large cyclones.

Boundary-Layer Meteorology **61**: 13–46, 1992.

The cold and dry air from the ice or land surface is rapidly heated and moistened over the water. The initial, dynamically influenced character of the boundary layer changes to a convectively influenced one, resulting in an increase of boundary-layer depth with increasing distance from the ice edge or coast.

In most cases, roll-like secondary flow circulations with aspect ratios (wavelength vs. depth) of around 3:1 develop in the boundary layer. If the boundary layer grows higher than the lifting condensation level, clouds mark the upward branches of the roll circulation in the form of cloud streets oriented about parallel to the mean boundary-layer flow. The roll wavelength usually increases downstream at a higher rate than the depth of the boundary layer (e.g., Miura, 1986). After a region of transition, the longitudinal cloud structures change in many cases to open or closed cellular structures. These cloud patterns are characteristic of cold air outbreaks in middle latitudes far from the cold air source.

The air–sea temperature difference ΔT amounts to $-20\,°K$ in extreme cases of cold air outbreaks described in the literature (e.g., Hein and Brown, 1988). In this paper, a moderate to weak cold air outbreak over the Greenland Sea west of Spitsbergen (Figure 1) on 15 and 16 May 1988 is presented, where ΔT was not more than $-5\,°K$. The objectives of the study are to investigate the downstream modification of boundary-layer structure, fluxes and cloud cover.

The depth of the boundary layer increased relatively slowly in the downstream direction. Clouds in the boundary layer were already present at the ice edge. The downstream development of cloudiness over the open water depended very sensitively on the moisture amount above the inversion. On 15 May, when the moisture was low above the inversion, clouds dissolved over the open water but developed again farther downstream, whereas on 16 May, when the moisture was relatively high above the inversion, the cloud streets at the ice edge grew farther downstream to form closed longitudinal stratocumulus cloud structures.

The longitudinal cloud structures over the water near the ice edge were generated to a large extent by dynamical instability due to vertical wind shear at the inclined inversion. Although thermal generation compared to dynamical generation became increasingly important on the secondary flow over the open water, the wind shear effect at the inversion was still present and not negligible.

The observations on 16 May were taken as a basis for numerical simulations with a LES (Large Eddy Simulation) model by Chlond (1992). The model results clearly emphasise the importance of the high moisture content above the inversion for the development of cloud and the importance of wind shear near the inversion for secondary flow generation.

2. Data and Large-Scale Weather Situation

The measurements for this investigation were taken on 15 and 16 May during the field experiment ARKTIS 1988 which took place over ice and water in the area west of Spitsbergen during the period 5 to 27 May 1988 (Figure 1). In order to

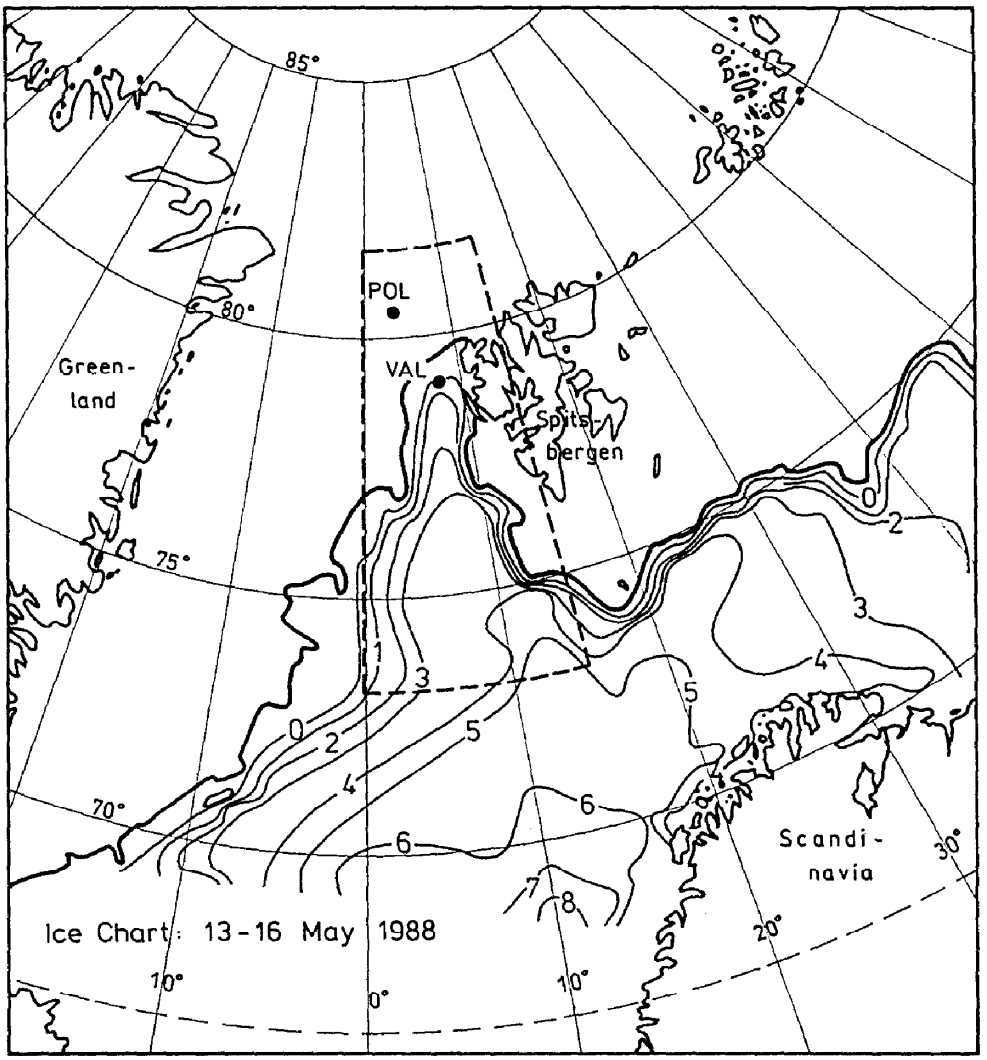

Fig. 1. Area of the field experiment ARKTIS 1988 during the period 5 to 27 May 1988 (dashed line). Dots mark the average positions of the research vessels POLARSTERN and VALDIVIA. The thick line gives the extreme location of the drift ice border and the thin lines are sea surface temperature isolines during the period 13 to 16 May 1988. Ice and temperature charts are obtained from Det Norske Meteorologiske Institutt, Oslo.

study off-ice and on-ice air flows, the research icebreaker POLARSTERN was situated about 100 km within the ice and the research vessel VALDIVIA in the open water some distance from the ice edge. At both ships, intensive surface observations and four-hourly radiosonde ascents were made.

Four research aircraft operated from the airfield Longyearbyn on Spitsbergen: a FALCON-20, a DORNIER-128 and two DORNIER-228. FALCON-20 and DORNIER-128 were equipped with gust probes to measure mean and turbulent

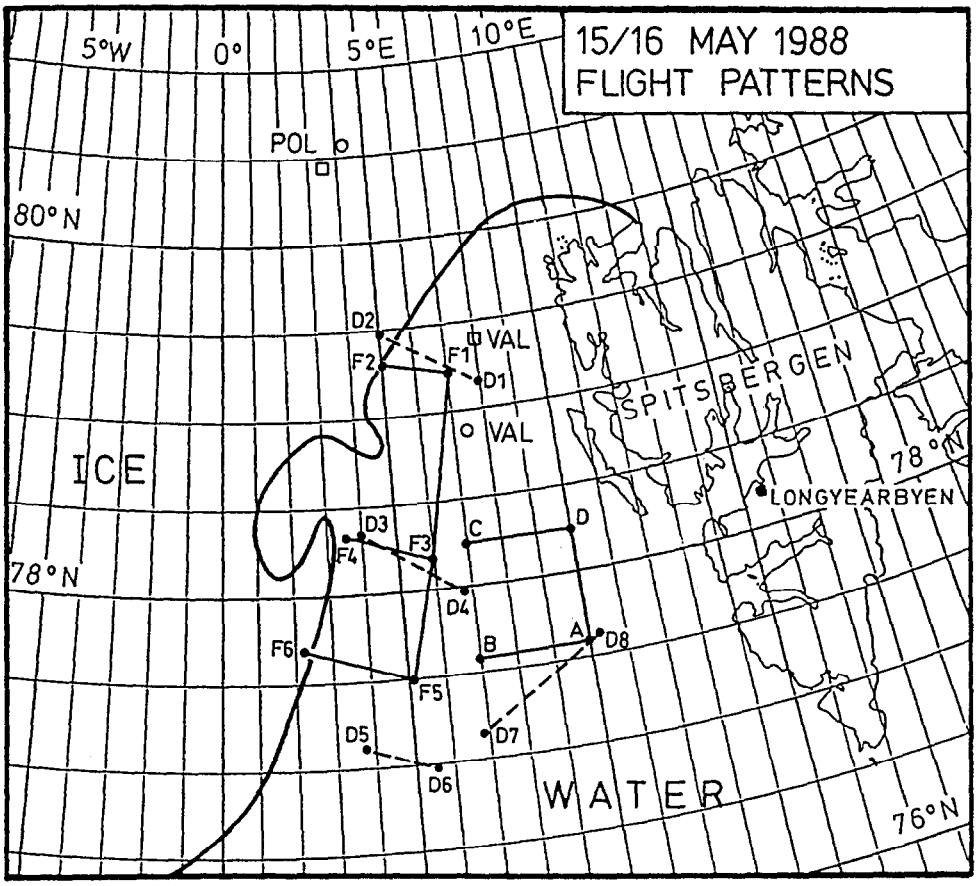

Fig. 2. Flight patterns of the research aircraft FALCON (A–D) on 15 May and FALCON (F1–F6) and DORNIER-128 (D1–D8) on 16 May 1988. Open circles and open squares mark the positions of the research vessels POLARSTERN and VALDIVIA on 15 and 16 May, respectively. The thick full line marks the ice edge.

meteorological quantities and with a radiation thermometer to measure the surface temperature. FALCON furthermore measured short- and longwave radiation fluxes from above and below as well as droplet spectra by means of a FSSP-Knollenberg probe.

One of the two DORNIER-228 (D-CALM) was equipped with a downward facing LIDAR system to measure cloud top heights and the other (POLAR-2) with sensors to measure mean meteorological quantities and radiation fluxes. A NOAA satellite receiving station for AVHRR data was installed on the airfield Longyearbyn during the period of the experiment. Further details on the experiment and the platforms are given in Brümmer (1989).

The flight patterns of the aircraft missions on 15 and 16 May 1988 are presented in Figure 2, together with the location of the ice edge. The FALCON measure-

ments on 15 May took place between 09 and 12 UT at 90, 210 and 510 m along the line A-B, at 90 m height along A-D and at 90 and 210 m height along C-D. Vertical soundings were flown in the vicinity of the four corner points.

On 16 May, the FALCON measurements took place between 1630 and 1900 UT at 90 m height along the pattern labelled by F1 to F6 and additionally at 210 m along the short east-west oriented branches of the flight pattern. Vertical profiles were flown at the six corner points. The DORNIER-128 flight legs at 90 m height between 1430 and 1800 UT on this day are labelled D1 to D8.

On both days, the FALCON measurements were accompanied by simultaneous LIDAR measurements of the D-CALM flying at 3 km.

The cold air outbreak lasted from 15 until 17 May. In this paper only the period from 15 to 16 May is studied in detail, when the aircraft operated in the area. Figures 3a and b show the surface weather maps at 12 UT on 15 and 16 May, respectively. High pressure over Greenland and low pressure over the Barents Sea led to a northeasterly geostrophic flow in the experimental area west of Spitsbergen. On 15 May 1988 this flow did not extend far in the southwesterly direction due to a blocking low near Jan Mayen. On the next day, this low intensified and moved southeast towards the Norwegian coast so that a northeasterly geostrophic flow was present over large areas of the North Polar Sea.

The cloud situation in the experimental area is illustrated by NOAA-9 satellite images at 0948 UT on 15 May and at 1301 UT on 16 May (Figures 4a and b). On both days, a thin cloud deck was present over the ice near the northwestern corner of Spitsbergen. On 15 May, the clouds dissolved over the open water and formed again about 150 km farther downstream in the experimental area. On 16 May, the clouds near the ice edge were organized in strips which grew to form closed cloud structures.

The water temperature in the experimental area is influenced by the West Spitsbergen current which transports warm water northward. This leads to a far northward location of the ice edge and to positive water temperatures up to 79 °N (Figure 1). The aircraft measurements took place near the center of the warm water current.

Figure 5 illustrates the time development of temperature T, specific humidity q, wind speed FF and wind direction DD during the cold air outbreak episode at VALDIVIA based on the four-hourly radiosonde ascents. The episode began in the morning hours of 15 May with a wind shift from northwest to northeast. The cold air mass at VALDIVIA was only 300 to 400 m deep. The lowest air temperature occurred during forenoon of 16 May and led to air–sea temperature differences of -5 °K. On 15 May, the cold air was capped by a weak inversion and dry air above. One day later, warm and moister air was advected above the inversion from the easterly direction. The differential advection below and above the inversion caused a relatively unusual moisture profile with a humidity increase above the inversion.

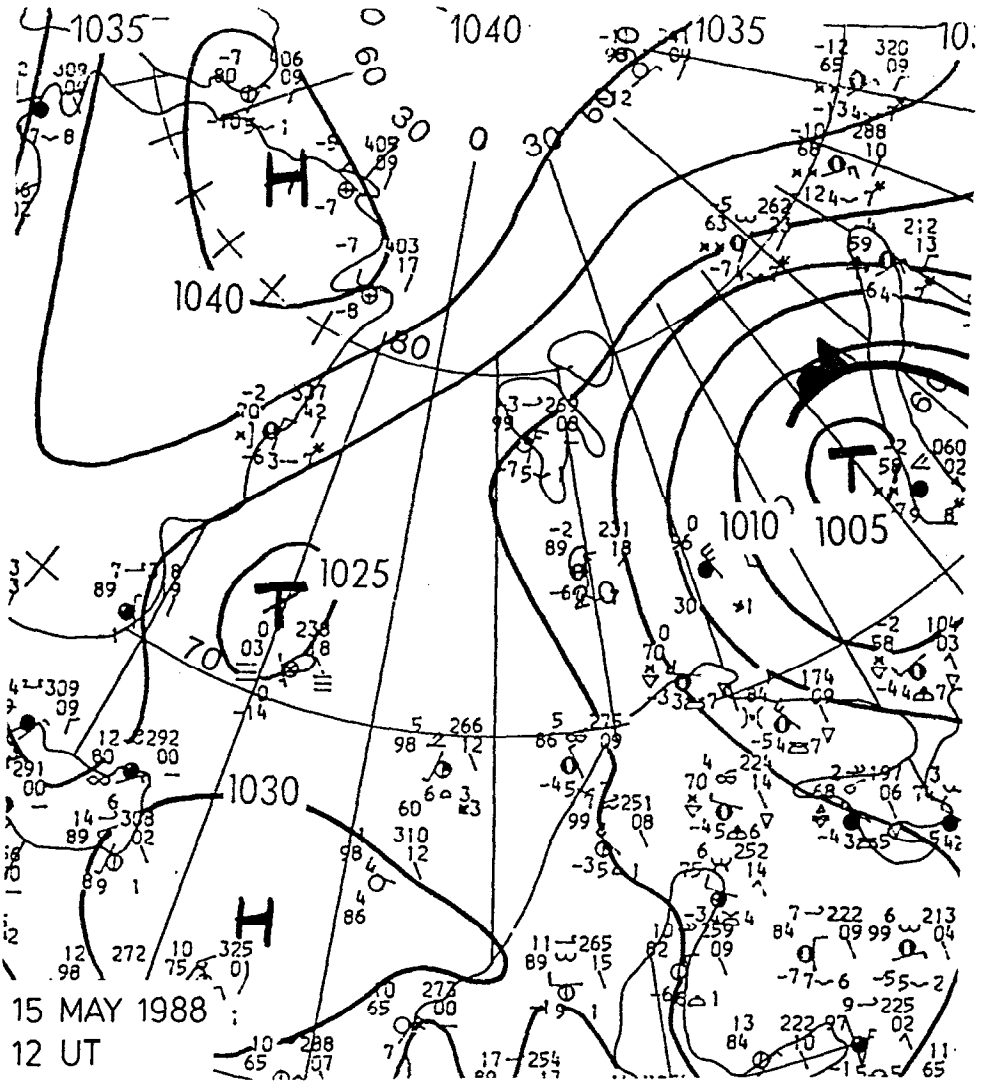

Fig. 3a. Surface weather chart on 15 May 1988 at 12 UT as published by Deutscher Wetterdienst, Offenbach.

3. Downstream Boundary-Layer Modification

3.1. Mean horizontal and vertical structure

The mean horizontal distribution of air and sea (T_w) temperature, water vapour mixing ratio m, and horizontal wind vector $\mathbf{v}$ is determined from the FALCON flights at 90 m; the distribution of boundary-layer height h is estimated from profile soundings and LIDAR measurements. The results for 15 and 16 May are shown in Figures 6 and 7, respectively.

The T_w distribution on the mesoscale is rather unsmooth with many meanders.

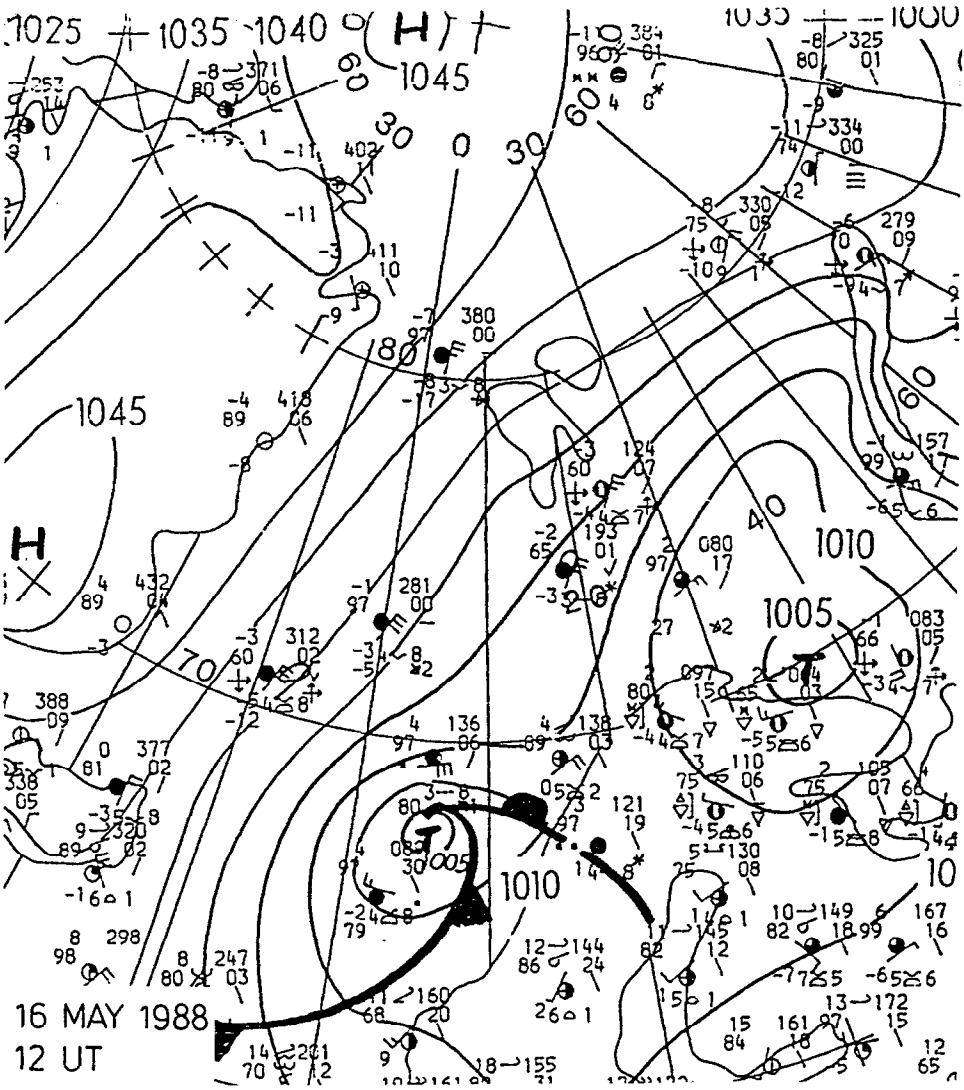

Fig. 3b. As Figure 3a, but for 16 May 1988.

The flight pattern on 15 May is located slightly to the right, and that on 16 May slightly to the left, of the center of the warm West Spitsbergen current. In contrast to T_w, the T distribution is much smoother. Beside the downstream temperature increase on both days, there is a T minimum coinciding with the center of the cloud field on 15 May and a decrease of T from east to west on 16 May. T increased downstream between 0.5 and 1.5 °K per 75 km on 15 May and about 3 °K per 200 km on 16 May. The m distribution roughly followed the T distribution; m increased downstream by between 0.05 and 0.12 g/kg per 75 km on 15 May and between 0.7 and 1.0 g/kg per 200 km on 16 May.

Wind speeds were between 10 and 16 m/s and the wind fields showed a weak

Fig. 4a. NOAA-9 satellite image (channel 2: visible) on 15 May 1988 at 0950 UT received in Longyearbyen by Deutsche Forschungsanstalt für Luft- und Raumfahrt. White lines mark FALCON flight pattern.

cyclonic curvature on both days. This latter fact may be a kind of lee-effect caused by the mountains of Northwest Spitsbergen.

The boundary-layer depth h increased downstream, but the h isolines were not aligned perpendicular to the wind. On 15 May, h was largest in the middle of the cloud field and decreased towards northeast and northwest, and on 16 May h increased from northeast to southwest. The crosswind inclination of h on 16 May appeared to be already present over the ice.

The vertical structure of T, m and the horizontal wind components u and v which are taken parallel and normal to the mean boundary-layer wind direction

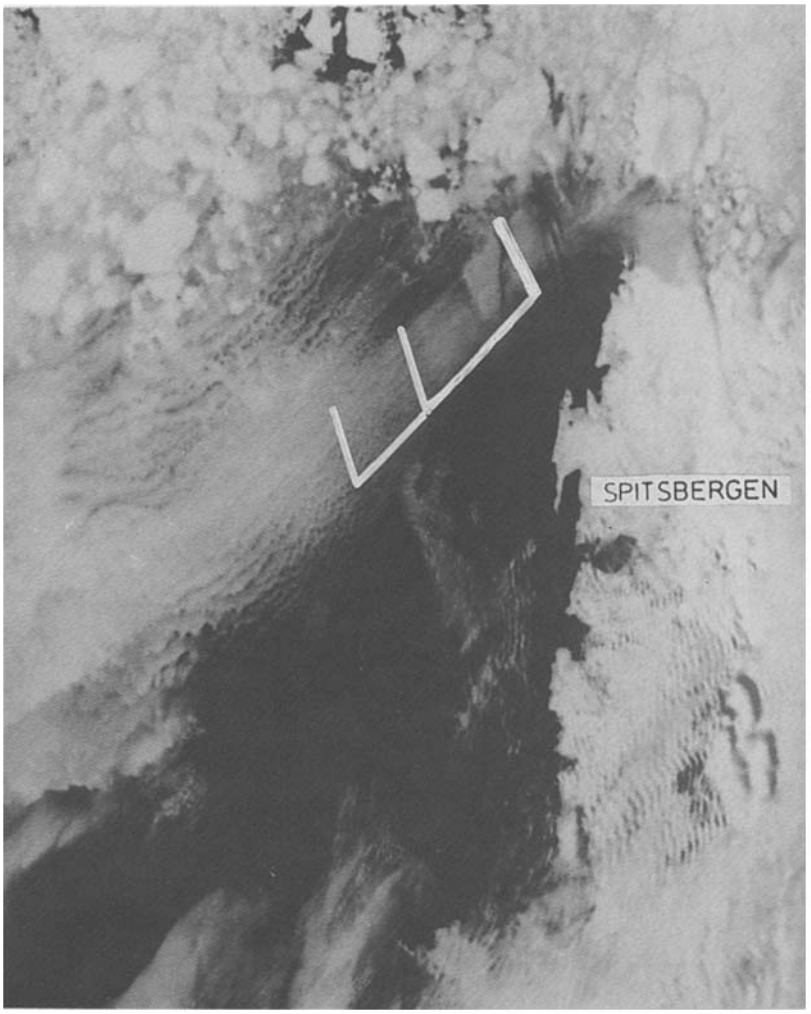

Fig. 4b. As Figure 4a, but for 16 May 1988 at 1301 UT.

is presented for both days in Figures 8 and 9, respectively. On 15 May, the boundary layer was capped by a weak inversion with a temperature increase of 0.5 to 1.5 °K. The moisture decreased at the inversion and remained small at higher levels. On 16 May, the inversion was much stronger (3 to 6 °K) and the moisture is small in the stable layer but relatively high above. This structure was present in the north part of the area at F1 and F2. Farther downstream in the southwest part, where the downstream increase of the boundary layer has bridged the original moisture minimum, a rather unusual moisture structure with a sharp moisture increase at the inversion is observed (at F4 and F6).

If the T profiles in the north part are compared with those in the south part of the flight area on 16 May, it is obvious that the downstream T increase in the

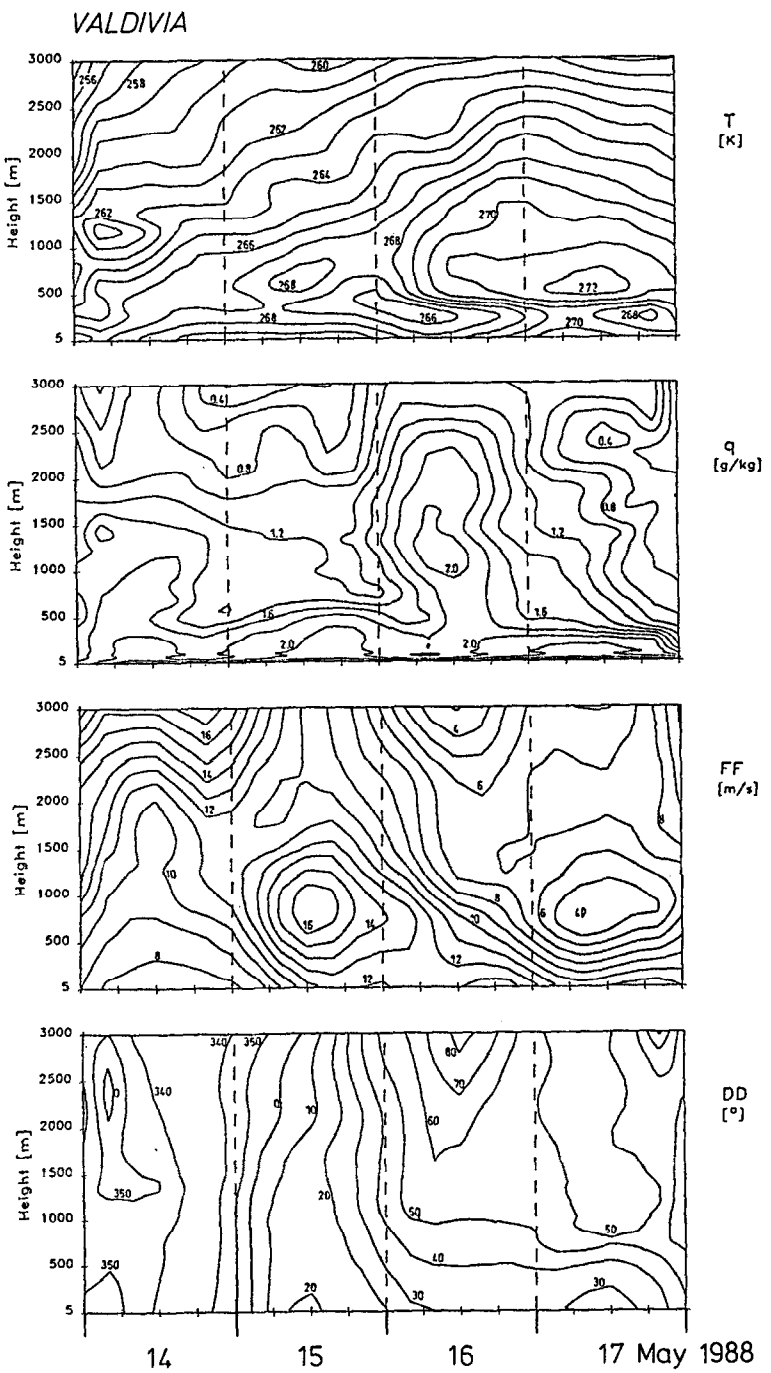

Fig. 5. Time-height cross-sections of temperature T, specific humidity q, wind speed FF, and wind direction DD based on four-hourly radiosonde ascents at VALDIVIA.

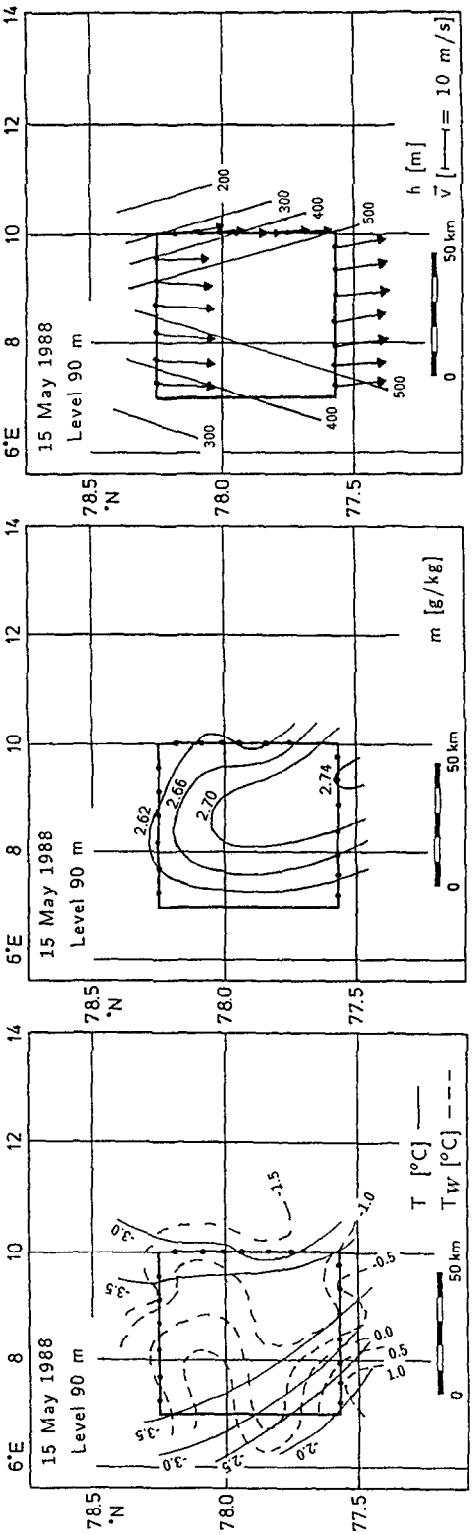

Fig. 6. Horizontal distribution of air and water temperature T, T_w (a), water vapour mixing ratio m (b) and wind vector $\mathbf{v}$ and boundary-layer height h (c) constructed from 10 km average values (dots) measured at 90 m height by FALCON on 15 May 1988. h isolines are based on profile soundings and LIDAR measurements.

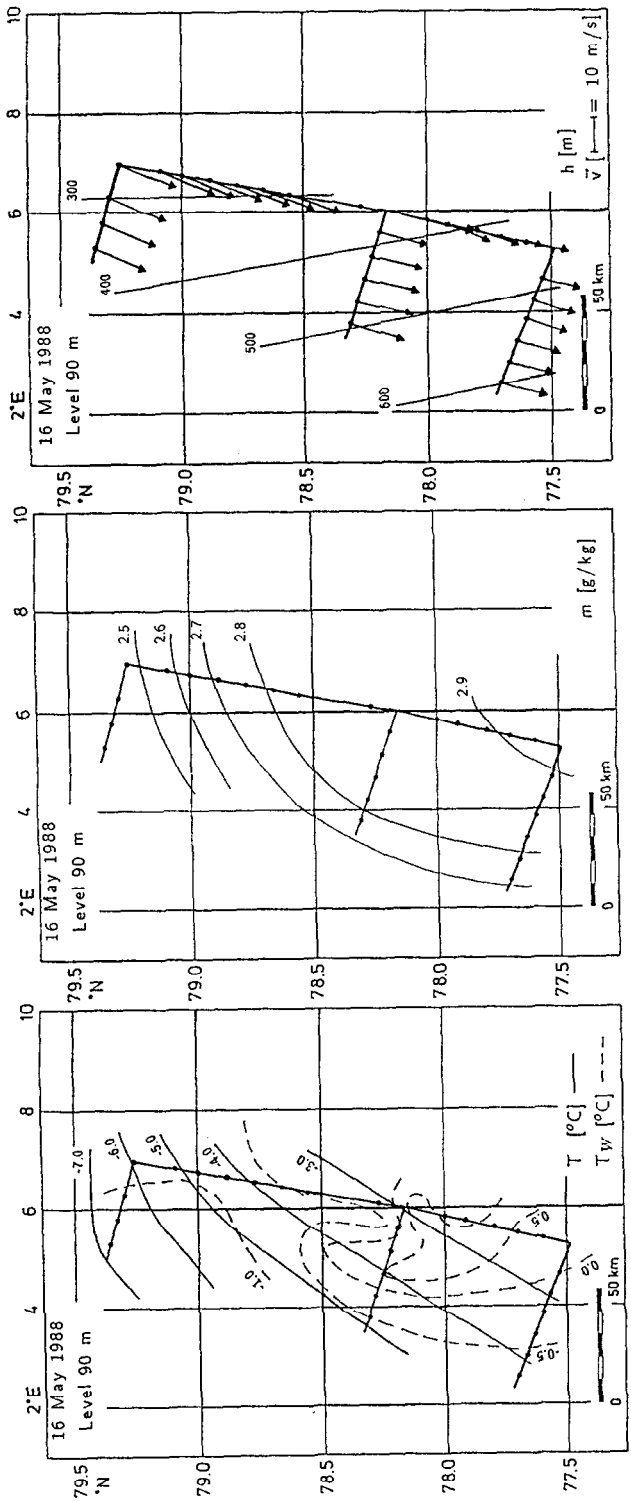

Fig. 7. As Figure 6, but for 16 May 1988.

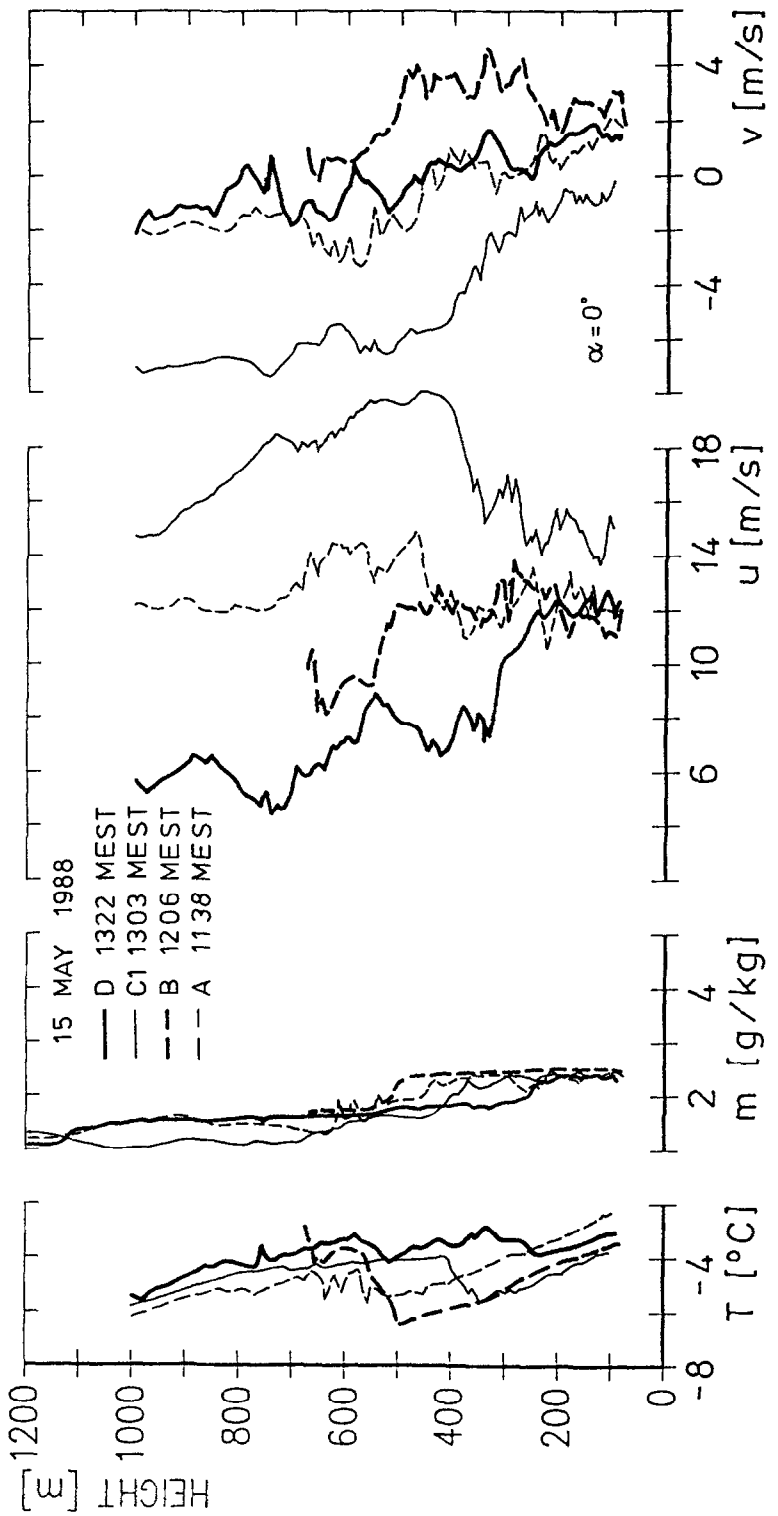

Fig. 8. Vertical profiles of temperature T, water vapour mixing ratio m, and wind components parallel (u) and normal (v) to the mean boundary-layer wind direction α measured by FALCON at corner points A–D on 15 May 1988.

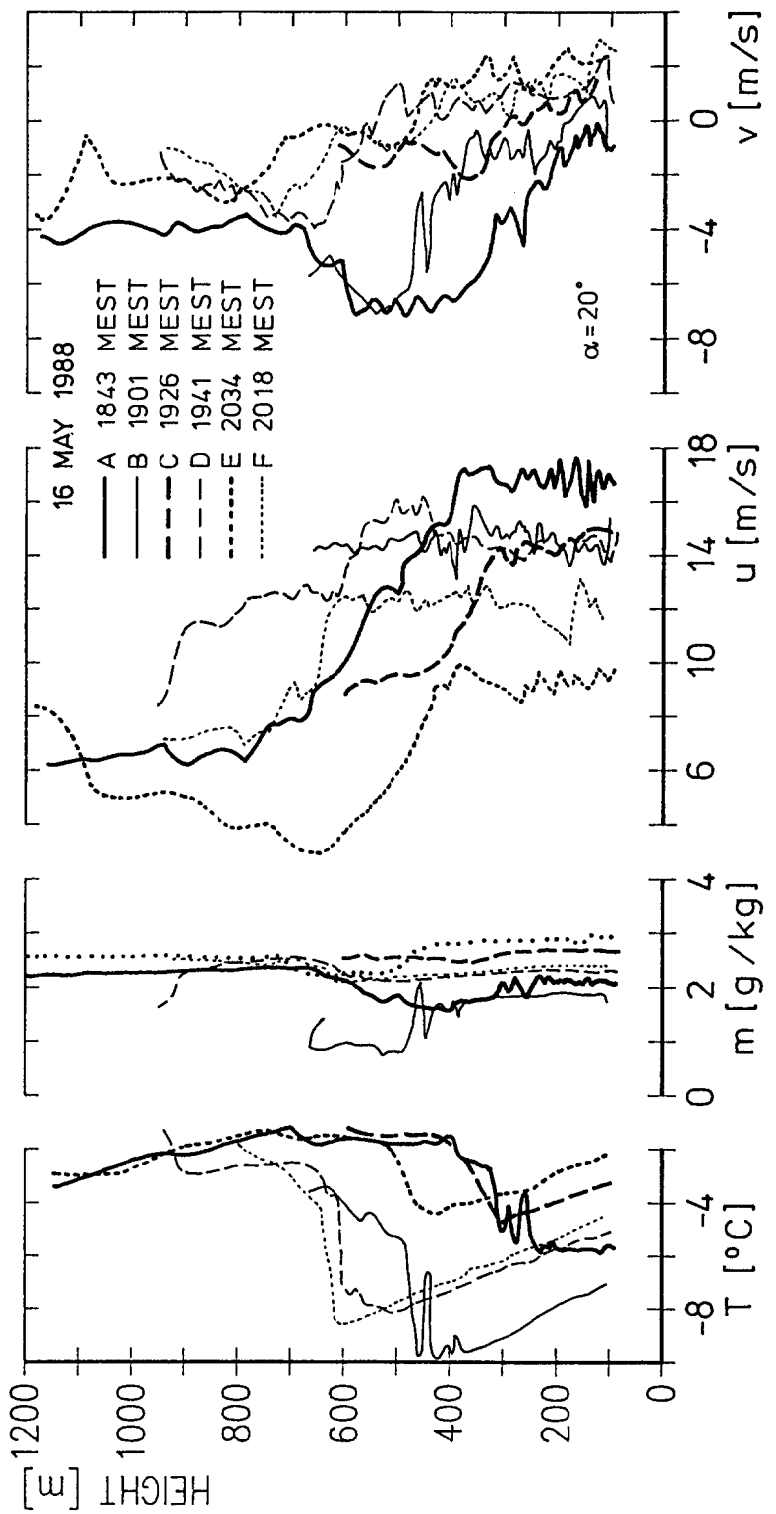

Fig. 9. As Figure 8, but for 16 May 1988.

boundary layer is to a large extent due to entrainment of warm air from the inversion. This is also true for the west branch of the flight area on 15 May. This suggests that entrainment heating is as important as, e.g., surface heating.

The u and v wind shears at the inversion as shown in Figures 8 and 9 are in accordance with the baroclinicity due to the inclined inversion: the downwind increase of h results in a decrease of v at the inversion and the crosswind inclination leads either to an increase of u at the inversion (as obvious in the profiles at the west side of the flight pattern on 15 May) or to a decrease of u (as obvious in the profiles at the east side of the flight pattern on 15 May and in all profiles on 16 May). This leads to inflection points in all u and v profiles in the vicinity of the inversion base, a necessary condition for the generation of inflection-point instability. The wind shear near the inflection points ranges from $2 \cdot 10^{-2}\,s^{-1}$ to $11 \cdot 10^{-2}\,s^{-1}$ and is about $5 \cdot 10^{-2}\,s^{-1}$ on average for both components.

3.2. Turbulent structure

Turbulent fluxes of sensible heat H, latent heat E, u-momentum τ_x and v-momentum τ_y have been calculated from the data observed on the horizontal flight legs by the formulae:

$$H = \rho c_p \overline{w'\Theta'}, \quad E = \rho L \overline{w'm'}, \quad \tau_x = \rho \overline{w'u'} \quad \text{and} \quad \tau_y = \rho \overline{w'v'}, \qquad (1)$$

where ρ, L and c_p are the density, latent heat of evaporation and specific heat at constant pressure, respectively. Before the correlations were calculated, linear trends over the 40 to 70 km long legs were removed. Figures 10 and 11 show the fluxes at 90 m height for 15 and 16 May, respectively.

On 15 May no significant downstream variations of the fluxes are observed. H and E at the alongwind flight leg are clearly smaller than at the crosswind legs because the alongwind leg is situated in a less convective region with only a few clouds and because contributions by wind-parallel secondary flow circulations are not sampled in a statistically significant manner on a wind-parallel flight leg.

The fluxes on 16 May decrease systematically downstream in accordance with the downstream decrease of wind speed. Along the nearly 200 km long distance between the northern and southern FALCON crosswind flight leg, H decreases from values around $60\,W/m^2$ to less than $30\,W/m^2$, E from about $80\,W/m^2$ to $40\,W/m^2$ and τ_x from about $-0.2\,N/m^2$ to about $-0.1\,N/m^2$, while τ_y varies around zero.

The DO-128 fluxes on 16 May, although measured about two hours earlier than the FALCON fluxes, fit relatively well into the horizontal distribution of fluxes. This and the satellite images of this day suggest that the weather situation was approximately stationary. The H flux at the SE leg of DO-128 agrees well with the nearly vanishing air-sea temperature difference in this area (T_W measured by radiometer and T extrapolated adiabatically downward).

The vertical distribution of fluxes is shown in Figure 12. Due to limited aircraft endurance, the fluxes could be measured at three, respectively, two levels only.

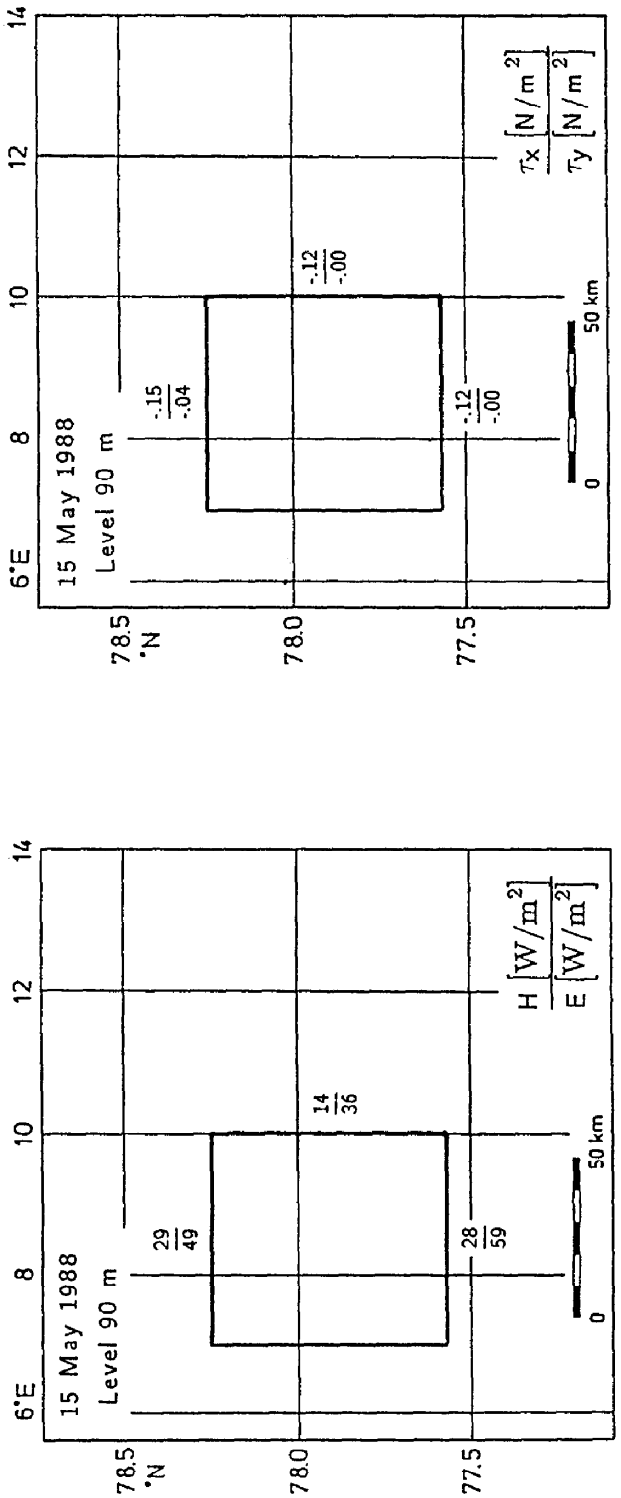

Fig. 10. Horizontal distribution of sensible (H) and latent heat flux (E), and alongwind (τ_x) and crosswind momentum flux (τ_y) measured by FALCON at 90 m height on 15 May 1988. Fluxes refer to the total length of the corresponding flight leg.

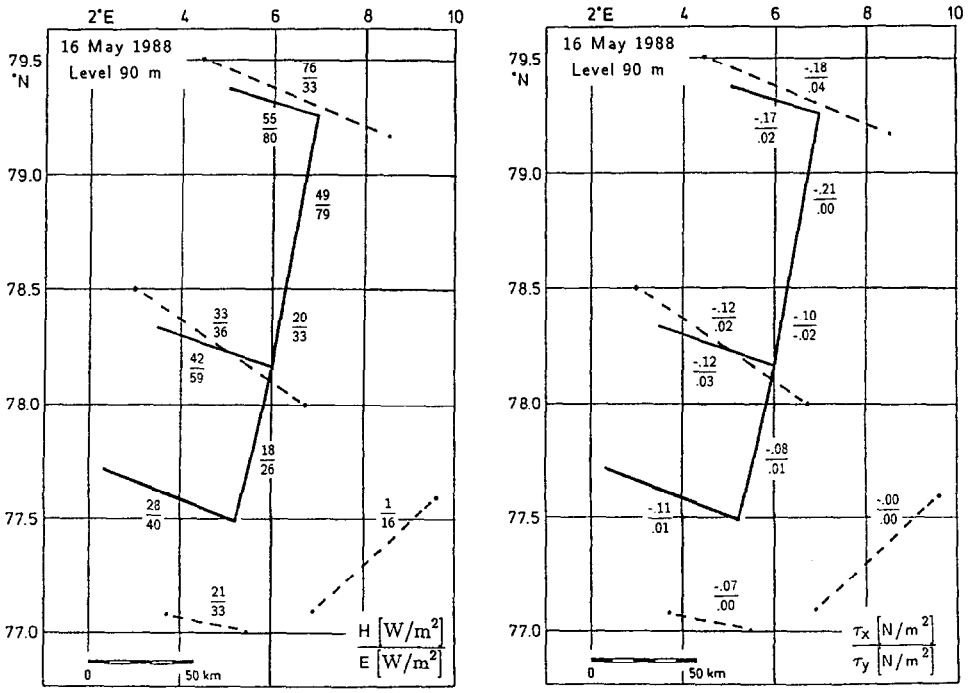

Fig. 11. As Figure 10, but for 16 May 1988. Full lines mark FALCON flight pattern and dashed lines DORNIER-128 flight pattern.

The flight legs at 90 m were all below cloud base, those between 200 and 250 m were near cloud base (partly below and partly in cloud) and that at 510 m on 15 May was mostly above the clouds. As for the horizontal flux distribution at 90 m, the flux profiles also are not significantly different between the north and the south leg on 15 May, whereas a systematic decrease from north to south is present in the subcloud layer on 16 May. The flux divergence in the subcloud layer is nearly the same on both days. The average values are about $-10 \cdot 10^{-2}\,\mathrm{W/m^3}$ for $\partial H/\partial z$, about $-9 \cdot 10^{-2}\,\mathrm{W/m^3}$ for $\partial E/\partial z$ about $0.05 \cdot 10^{-2}\,\mathrm{N/m^3}$ for $\partial \tau_x/\partial z$ and about $0.02 \cdot 10^{-2}\,\mathrm{N/m^3}$ for $\partial \tau_y/\partial z$.

3.3. Energy balance at the sea surface

The energy balance B at the sea surface is given by

$$B = R - H - E\,, \tag{2}$$

where R is the net radiation flux defined as

$$R = S\downarrow - S\uparrow + L\downarrow - L\uparrow\,, \tag{3}$$

and $S\downarrow$, $S\uparrow$, $L\downarrow$ and $L\uparrow$ are the shortwave and longwave downward and upward radiation fluxes, respectively. The sea surface receives energy if B is positive. Table I shows the flux components in (2) and (3) for the five crosswind flight legs at 90 m on 15 and 16 May. It is assumed that the conditions measured

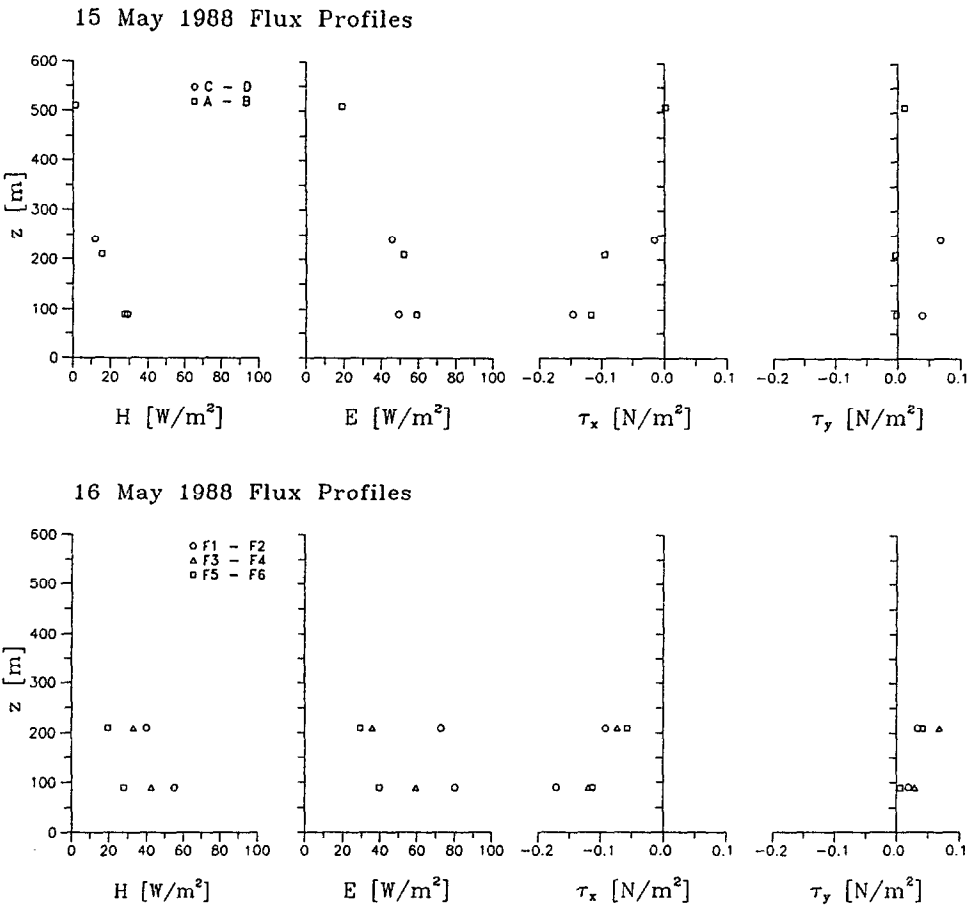

Fig. 12. Vertical fluxes of sensible (H) and latent heat (E) and alongwind (τ_x) and crosswind momentum (τ_y) measured by FALCON on crosswind flight legs A–B (□) and C–D (○) on 15 May 1988 (above) and legs F1–F2 (○), F3–F4 (△) and F5–F6 (□) on 16 May 1988 (below). Fluxes refer to the total length of the corresponding flight leg.

TABLE I

Radiation balance, $R = S\downarrow - S\uparrow + L\downarrow - L\uparrow$, and energy balance, $B = R - H - E$, at 90 m height at different distances Δx from the ice edge on 15 and 16 May 1988. N is the low-level cloud coverage

	Δx [km]	N	$S\downarrow$	$S\uparrow$ [W/m²]	$L\downarrow$	$L\uparrow$	R	$-H$ [W/m²]	$-E$	B
15.5.88	165	2/8	422	21	243	300	344	−29	−49	266
	225	4–5/8	337	16	262	304	279	−28	−59	192
16.5.88	50	3–4/8	279	30	232	292	189	−55	−80	54
	170	8/8	82	5	282	300	62	−42	−59	−39
	250	8/8	59	3	288	302	42	−28	−40	−26

at 90 m are not too different from those at the sea surface, although the magnitudes of H and E are slightly underestimated according to the flux profiles in Figures 12a and b and according to the observational fact that the flux gradients are approximately constant in the subcloud layer under unstable conditions (e.g., Chou and Ferguson, 1991).

The energy balance is substantially influenced by the degree of cloud cover N which increases on both days from north to south. In the case of small N, $S\downarrow$ is the dominating term; it determines the sign of B, as for example at the north leg on 16 May, where N is about 3-4/8. Here, the ocean is heated in spite of the large sensible and latent heat losses. Farther downstream, where N is 8/8, the heat fluxes dominate and the ocean is cooled. The measurements on 15 and 16 May were made during daytime conditions at different sun elevations. It is obvious from Table I that the degree of cloud cover has the opposite influence on the energy balance in the case of small sun elevations or at night. In this case, a clear sky will enhance energy loss of the sea surface during a cold air outbreak, more so than an overcast sky.

3.4. Temperature and moisture budget of the boundary layer

The downstream variation of potential temperature Θ and water vapour mixing ratio m in the boundary layer following an air volume are described by the following equations:

$$\frac{\mathrm{d}\tilde{\bar{\Theta}}}{\mathrm{d}t} = \frac{1}{h}\frac{\mathrm{d}h}{\mathrm{d}t}(\bar{\Theta}_h - \tilde{\bar{\Theta}}) - \frac{1}{h}(\overline{w'\Theta'})_h + \frac{1}{h}(\overline{w'\Theta'})_0 + \\ + \frac{L}{c_p h}\frac{\mathrm{d}}{\mathrm{d}t}(Nlh_c) + \frac{1}{\rho c_p h} N\,\Delta R_{L,n}\,, \tag{4}$$

$$\frac{\mathrm{d}\tilde{\bar{m}}}{\mathrm{d}t} = \frac{1}{h}\frac{\mathrm{d}h}{\mathrm{d}t}(\bar{m}_h - \tilde{\bar{m}}) - \frac{1}{h}(\overline{w'm'})_h + \frac{1}{h}(\overline{w'm'})_0 - \frac{1}{h}\frac{\mathrm{d}}{\mathrm{d}t}(Nlh_c)\,. \tag{5}$$

In (4) and (5) the overbar denotes a horizontal average in the crosswind direction (e.g., along a flight leg) and the tilde a vertical average from the surface to the top of the boundary layer. The first term on the right sides gives the effect of a change of boundary-layer depth in the case of a vertical temperature or moisture gradient in the boundary layer. The second and third terms represent the changes caused by entrainment fluxes and surface fluxes, respectively. The fourth term represents the effect of net-condensation, where l is the average liquid water content and h_c the depth of the cloud layer. Finally, the fifth term represents the effect of radiation flux divergence, where $\Delta R_{L,n}$ is the net longwave radiation flux difference between cloud top and cloud base, which is assumed to give the main contribution to the total radiation flux divergence.

The values of the individual parameters in (4) and (5) at the northern, middle

TABLE II

Average values on the north, middle and south leg of the FALCON flight pattern on 16 May 1988 entering into the determination of the individual terms of the temperature and moisture budget Equations (4) and (5): h boundary-layer depth; $\tilde{\bar{\Theta}}, \tilde{m}$ vertical averages of potential temperature and water vapour mixing ratio in the boundary layer; $\bar{\Theta}_h$, $\tilde{m}_h$ corresponding values at boundary-layer top; u downstream wind component; Δx approximate distance from ice edge; N cloud cover; l liquid water content; h_c cloud layer depth; $(\overline{w'\Theta'})_0$, $(\overline{w'm'})_0$ surface fluxes of temperature and moisture; and $\Delta R_{L,n}$ net longwave radiation flux difference between cloud top and base

	h	$\tilde{\bar{\Theta}}$	$\bar{\Theta}_h$	$\tilde{m}$	$\tilde{m}_h$	u	Δx
North	350	−8.0	−7.6	1.93	1.90	15.5	50
Middle	480	−5.5	−5.2	2.43	2.35	14.3	170
South	550	−4.6	−4.3	2.57	2.40	10.5	250
	m	°C	°C	g/kg	g/kg	m/s	km

	N	l	h_c	$(\overline{w'\Theta'})_0$	$(\overline{w'm'})_0$	$\Delta R_{L,n}$
North	4/8	0.01	170	0.050	0.026	−35
Middle	8/8	0.03	300	0.038	0.023	−35
South	8/8	0.05	370	0.026	0.016	−35
		g/kg	m	m/s · K	m/s · g/kg	W/m^2

and southern crosswind flight sections on 16 May are listed in Table II. The values of h, $\tilde{\bar{\Theta}}$, $\bar{\Theta}_h$, $\tilde{m}$, $\tilde{m}_h$ and h_c are taken from Figure 9, the surface fluxes from Figure 12 by linear extrapolation to the sea surface, l from Figure 14c, $\Delta R_{L,n}$ from Figure 15 and N from eye observations. The time interval dt in (4) and (5) is estimated from the assumption $dt = dx/u$, where dx is the downstream distance between the crosswind flight legs and u the average downstream wind component. Since u does not vary much with height in the boundary layer (Figure 9), this assumption is approximately fulfilled. All terms in (4) and (5) can be determined from observations except the entrainment fluxes at the top of the boundary layer. These were calculated as residuals. The individual terms in (4) and (5) are given in Table III.

Temperature and moisture changes average 0.8 °K/h and 0.15 g/kg/h, respectively. They are about twice as large in the north part of the experimental area as in the south part. The downstream temperature increase is caused by heating from the sea surface and by entrainment. The latter predominates, being about two times larger than the former. The net radiation flux divergence, which is mainly given by the longwave radiation flux divergence in the vicinity of the cloud

because the vertical gradient of Θ is small in the boundary layer. Surface heating and entrainment heating decrease downstream whereas radiation cooling is about constant.

The downstream moisture increase is caused by evaporation from the surface. All other terms are clearly smaller and slightly negative. The surprisingly small

TABLE III

Values of the individual terms of the temperature and moisture budget in the boundary layer on 16 May 1988. See Table II and text for explanation of symbols. The accuracy of the residual entrainment fluxes is estimated as 0.1 to 0.2 K/h for $1/h\ (w'\Theta')_h$ and as 0.05 g/kg/h for $1/h\ (w'm')_h$

16 May 1988	$\frac{d\bar{\tilde{\Theta}}}{dt}$	$\frac{1}{h}\frac{dh}{dt}(\bar{\Theta}_h - \bar{\tilde{\Theta}})$	$-\frac{1}{h}(\overline{w'\Theta'})_h$	$\frac{1}{h}(\overline{w'\Theta'})_0$	$\frac{L}{c_p h}\frac{d}{dt}(Nlh_c)$	$\frac{1}{\rho c_p h} N\Delta R_{L,n}$
North → Middle	1.11	0.05	0.83	0.38	0.02	−0.17
Middle → South	0.51	0.03	0.42	0.22	0.03	−0.19
			°K/h			
16 May 1988	$\frac{d\bar{\tilde{m}}}{dt}$	$\frac{1}{h}\frac{dh}{dt}(\bar{m}_h - \bar{\tilde{m}})$	$-\frac{1}{h}(\overline{w'm'})_h$	$\frac{1}{h}(\overline{w'm'})_0$	$-\frac{1}{h}\frac{d}{dt}(Nlh_c)$	
North → Middle	0.22	−0.01	0.03	0.21	−0.01	
Middle → South	0.08	−0.01	−0.03	0.13	−0.01	
			g/kg/h			

TABLE IV

Cloud base z_B, cloud top z_T, cloud coverage N and cloud type C_L observed by eye during the FALCON profile soundings on 15 and 16 May 1988

		West Side				East Side			
		Z_B [m]	Z_T [m]	N	C_L	Z_B [m]	Z_T [m]	N	C_L
15.5.88	North	240–270	350–420	2/8	Cu	–	–	0/8	–
	South	360	500–650	4–5/8	Cu/Sc	240–280	510	8/8	Sc
16.5.88	North	210	450	4–5/8	Cu	130–170	250–300	2–4/8	Cu
	Middle	210	600	8/8	Sc/St	150	360–390	6/8	Sc
	South	180–210	630	8/8	Sc/St	150	480	8/8	Sc/St

magnitude of the drying due to entrainment is a consequence of the relatively high moisture content above the inversion. Under "normal" moisture profile conditions, this term can be on the order of minus one half of the surface flux.

The calculated values of the individual terms in (4) and (5) from the observations have of course associated errors due to instruments, assumptions (representativity of the profiles at the corner points), etc. All uncertainties will sum up in computations of residual terms. It is estimated that the largest uncertainty may originate from the determination of the terms on the left side of (4) and (5) on the order of 0.1 °K/h and 0.03 g/kg/h, respectively, and that the uncertainty of the other terms is on the order of 10% of their computed values. This results in uncertainties of the residual entrainment fluxes of about 0.15 K/h for 1/h $(\overline{w'\Theta'})_h$ and of about 0.05 g/kg/h for 1/h $(\overline{w'm'})_h$. These uncertainties will not affect the basic conclusions with respect to the residual terms and the relative magnitudes of the individual terms in the budget equations.

4. Characteristics of the Cloud Fields

4.1. Cloud coverage

The cloud situations in the experimental area on 15 and 16 May are summarized in Table IV, based on eye observations during the FALCON profile soundings. On both days, the cloud coverage increased downstream from broken to closed cloud cover. Simultaneously the cloud layer depth increased from less than 100 m to more than 400 m over a distance of 90 to 200 km and the cloud type changed from cumulus to stratocumulus or stratus.

northern and southern crosswind flight leg. The measurements show the mean increase of z_T in the downstream as well as east-west direction. For the southern flight leg, z_T variations over smaller distances can be more than 100 m. The z_T characteristics in Figure 13 look very similar to stratocumulus LIDAR measurements presented by Atlas *et al.* (1986) and Boers *et al.* (1988).

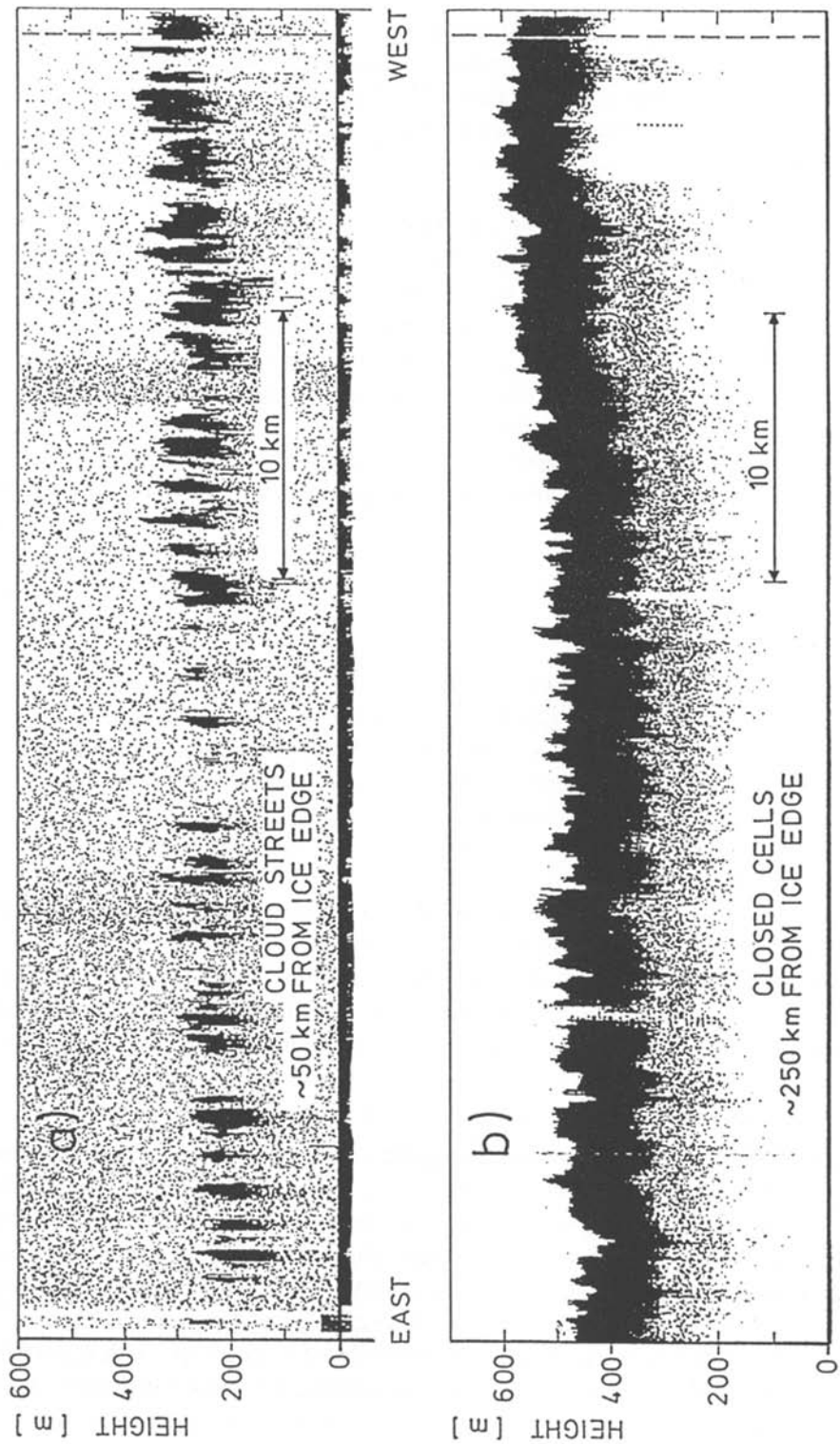

Fig. 13. Horizontal distribution of cloud top height z_T from LIDAR measurements of D-CALM from about 3 km altitude. Above: flight leg F1–F2 in the broken cloud region at about 50 km distance from the ice edge. Below: flight leg F5–F6 in the region of closed cloud cover at about 250 km distance from the ice edge. Pulse frequency: every second corresponding to every 100 m.

Eye observations and satellite images show that the broken cloudiness at the northern leg was organized in wind-parallel cloud streets while the closed cloudiness in the south had meander structures. The LES model calculations by Chlond (1991) with different vertical moisture profiles suggest that the rapid downstream increase of cloud cover was a result of the high moisture content above the inversion.

The development of cloud cover over the open water near the ice edge on 15 May is different from that on 16 May. The satellite image at 0948 UT on 15 May (Figure 4a) shows that clouds over the ice (8/8 stratus) dissolve when coming over the water and develop again about 150 km farther downstream in the experimental flight area. Two possibilities for cloud dissolution are imaginable: either entrainment of dry and warm inversion air causes a sub-saturation of the boundary-layer air or increased mesoscale divergence causes a sinking of the inversion base below the condensation level. Since the boundary layer over the warm water is heated from below and above and moistened from below but dried from above, it may result that

$$\frac{de}{dt} < \frac{de_s(T)}{dt}, \tag{6}$$

where e and $e_s(T)$ are the water vapour pressure and saturation water vapour pressure in the cloud layer, respectively. If (6) holds, the originally saturated air ($e = e_s$) will finally arrive at $e < e_s$ and consequently clouds will dissolve.

According to the first possibility, we would expect a downstream increase of h and according to the second possibility a downstream decrease of h. These hypotheses can be tested by profile measurements taken nearly simultaneously at point C by FALCON (at 1103 UT: $h = 400$ m), at VALDIVIA (at 0900 and 1200 UT: $h = 300$ and 380 m, respectively) and by POLAR-2 near 79.5° N, 07.0° E, about 70 km north of VALDIVIA (at 1130 UT: $h = 390$ m) (see Figure 2). Since these observations give no significant downstream change of h, it may be concluded that both processes are working. Unfortunately, the available measurements in this area are not sufficient to calculate the divergence field for a more detailed analysis.

4.2. Cloud properties and longwave radiation

The vertical profiles of cloud droplet concentration N_c mean droplet radius $\bar{R}_c$ and liquid water content l measured by the Knollenberg FSSP-probe on board the FALCON at locations F1 to F6 on 16 May are presented in Figure 14. Apart from the F1 profile through broken clouds, N_c has values around 100/cm^3 and decreases slightly from z_B to z_T. Also R_c shows a systematic variation: it is about 5 μm around z_B (150–200 m) and increases at a rate $\Delta R_c/\Delta z$ of 1–2 μm per 100 m.

N_c and R_c height variations result in a nearly linear increase of l with a gradient $\Delta l/\Delta z$ of about 0.2 g/kg per 100 m so that the maximum l value amounts to about 0.1 g/kg at 650 m height at point F6. The observed $\Delta l/\Delta z$ is smaller than the

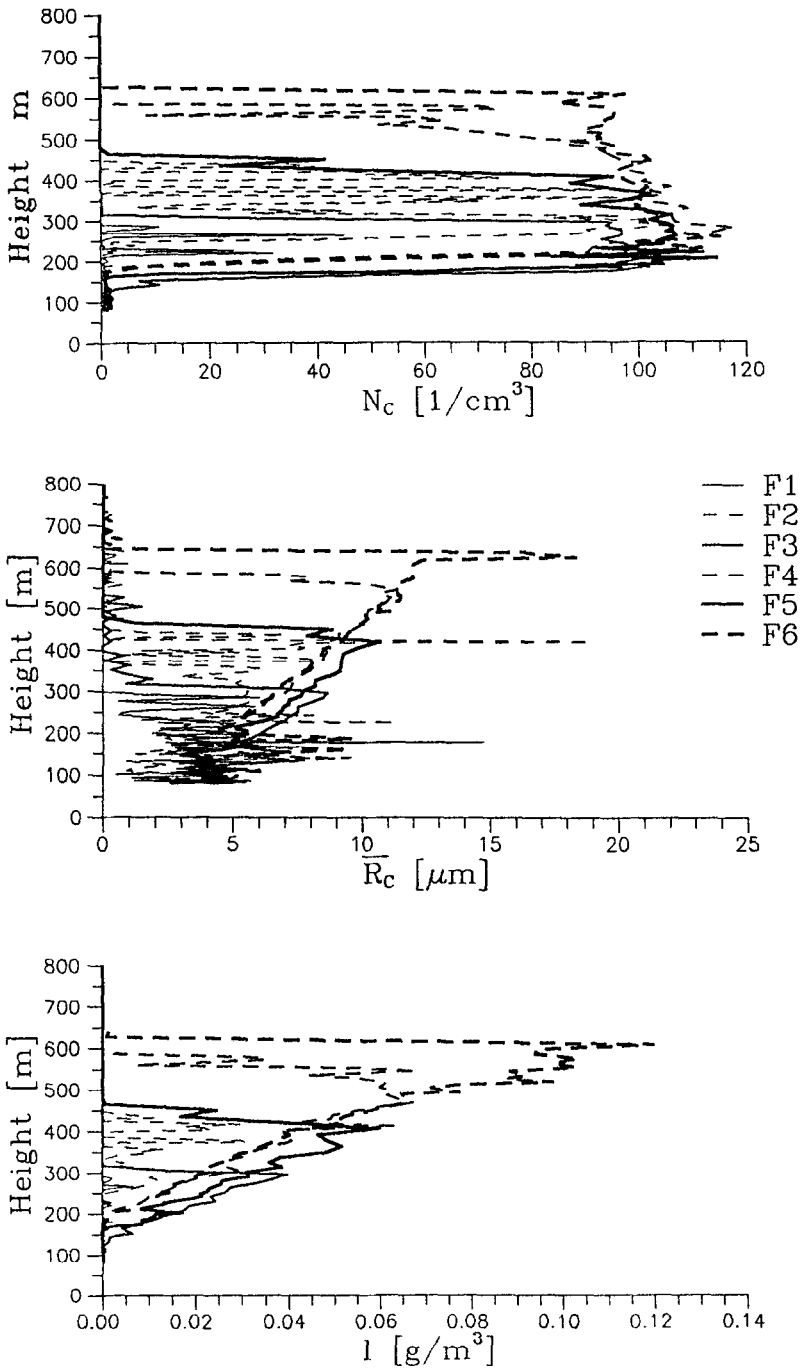

Fig. 14. Vertical profiles of cloud droplet concentration N_c mean droplet radius R_c and liquid water content l measured by the Knollenberg FSSP probe on board of FALCON at points F1 to F6 on 16 May 1988. The height is measured by radio altimeter.

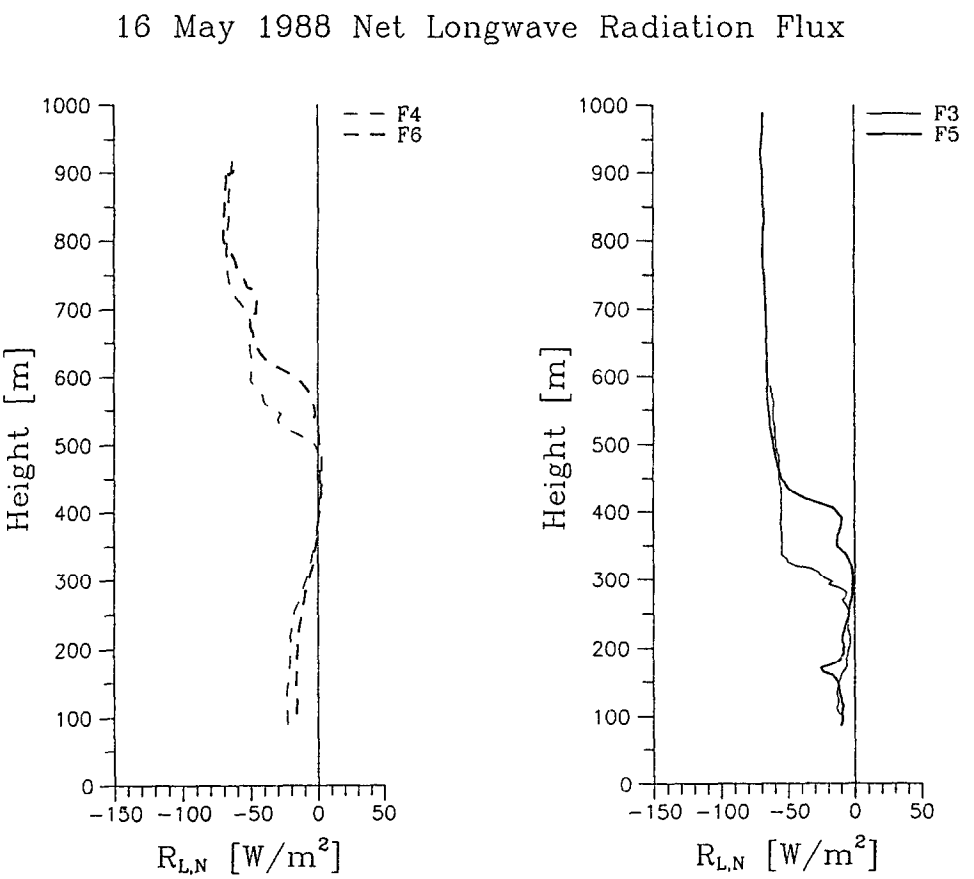

Fig. 15. Vertical profiles of net longwave radiation flux, $R_{L,n}$ measured by upward and downward facing pyrgeometers on board of FALCON at points F3 to F6 where a closed cloud deck is present on 16 May 1988. The height is measured by radio altimeter.

adiabatic value $(\Delta l/\Delta z)_{ad}$, which is about 0.1 g/kg per 100 m. It is interesting to mention that the observed $\Delta m/\Delta z$ in the cloud layer (Figure 9) which is between -0.05 and -0.1 g/kg per 100 m corresponds better to $(\Delta l/\Delta z)_{ad}$. Another independent sensor to measure l at the FALCON, a so-called King probe, gives l values which are nearly identical with those of the Knollenberg, so that the measured l appears to be correct. The reason for the large difference between observed and adiabatic l values is not exactly known, but presumably the difference is caused by cloud top entrainment which reduces l and increases m by evaporation and which reduces m by mixing (except at points F4 and F6, where m increases across the inversion).

Net longwave radiation fluxes $R_{L,n}$ in the cloud layer are presented in Figure 15. The profiles hold for points F3 to F6 where a closed cloud deck is present. On the average, the flux divergence $\Delta R_{L,n}/\Delta z$ is about -50 W m^{-2} over a 90 m deep layer at cloud top and about 13 W m^{-2} over a 150 m deep layer at cloud base.

Shortwave radiation fluxes R_s were also measured. However, since R_s depends very sensitively on a deviation of the aircraft z-axis from the z-axis in a fixed earth system, a careful correction is necessary. This correction was not yet finished at the time that this paper was written.

4.3. Cloud patterns

As mentioned above, on 16 May the cloud patterns in the experimental area changed from wind-parallel cloud streets in the northern part to closed meander cloud structures farther downstream (see Figure 4b). Such patterns are caused by secondary flow circulations rotating around horizontal, approximately wind-parallel roll axes, as shown in many experimental and model studies (e.g., LeMone, 1973; Chou and Ferguson, 1991). Since crosswind flights were made only at 90 and 210 m, the secondary flow should be represented best in the v-component at the lower flight level. Figure 16 shows the v-variance spectra at 90 m height for the three crosswind flight legs. The variance has a broad maximum in all three spectra which shifts with increasing distance x from the ice edge to smaller frequencies or equivalently to longer horizontal wavelengths if time is converted to space via the average flight speed of 100 m/s. The main characteristics of Figure 16 are summarized in Table V. The horizontal wavelength λ_{max}, at which the v-variance is maximum, has values around 1200 m at $\Delta x = 50$ km and increases to values between 3000 and 7000 m at $\Delta x = 250$ km. This corresponds to a downstream increase of the aspect ratio λ_{max}/h from 3.2 to values between 5.4 and 12.7. Thus the aspect ratio of the closed meander cloud structures is clearly larger than that of classical thermal Rayleigh instability, which is 2.8. A downstream increase of aspect ratio was also found by Miura (1986) and Kelly (1984).

Secondary flows can be driven by thermal and shear instability. The respective generation rates of kinetic energy are defined by

$$\frac{g}{\bar{\Theta}}\,\overline{w'\Theta_v'} \quad \text{and} \quad -\overline{w'v'}\,\frac{\partial \bar{v}}{\partial z}, \tag{7}$$

where g is the Earth's gravity and Θ_v the virtual potential temperature. In (7) the shear production $-\overline{w'u'}\,\partial\bar{u}/\partial z$ is not included because it does not contribute directly to the kinetic energy of the roll circulation in the vertical plane perpendicular to the roll axis which is approximately parallel to the mean boundary-layer wind direction.

In order to find the primary driving mechanism in this case, continuous vertical flux profiles in the boundary layer would be needed. Since horizontal flights at only two levels are available, we attempted to estimate the fluxes from the profile flights at F1 to F6. For that purpose, a profile flight was divided into 10 s (1 km) long subintervals for which linear trends were removed and then fluxes and variances were calculated. This procedure is justified because the aircraft climb rate is only between 165 and 330 m/min corresponding to inclination angles between

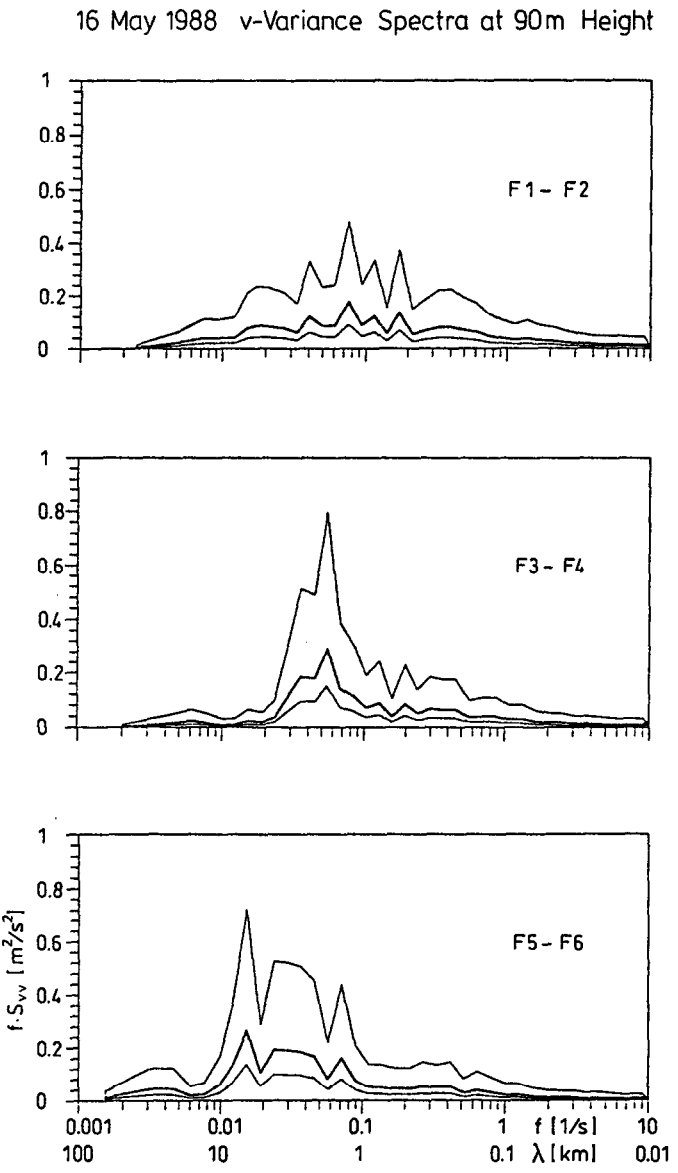

Fig. 16. Variance spectra of normal wind component v measured by FALCON at 90 m on flight legs F1–F2 (distance Δx from ice edge about 50 km), F3–F4 ($\Delta x \approx 170$ km) and F5–F6 ($\Delta x \approx 250$ km) on 16 May 1988. Thin lines give the 95% confidence limits. f is frequency and $\lambda = V_a/f$ is wavelength where V_a is the aircraft velocity.

1.4 and 2.8°. The limitation is that only contributions by motions with horizontal scales shorter than 1 km can be included. The fluxes and variances obtained from the individual profiles were averaged separately for profiles with a broken cloud cover at F1 and F2 and with a closed cloud cover at F3 to F6. Average fluxes and variances are shown in Figures 17 and 19, respectively.

TABLE V

Variation of horizontal wavelength λ_{max} of maximum v-variance at 90 m height and boundary-layer depth h with increasing distance Δx from ice edge on 16 May 1988

Δx [km]	z [m]	h [m]	z/h	λ_{max} [m]	λ_{max}/h
50	90	375	0.24	1200	3.2
170	90	480	0.19	2300	4.8
250	90	550	0.16	3000–7000	5.4–12.7

As in Figure 12 the fluxes are generally larger in the broken than in the closed cloud case (Figure 17). Particularly striking are the large values of $w'\Theta'$, $w'm'$ and $w'v'$ just below z_T in the broken cloud case emphazising the important role of entrainment. There, the sensible heat flux amounts to $-70\,W/m^2$ and has the same magnitude as the surface heat flux. The $w'v'$-flux near z_T is also remarkable because its magnitude is nearly 30% of the surface $w'u'$-flux.

The generation terms in (7) are shown in Figure 18. In the broken cloud case with cloud streets, the dynamical generation has a maximum near z_T. The thermal generation is only positive below z_B and has large negative values near z_T. Thus both generation mechanisms are acting. Averaged over the entire boundary layer, dynamical generation is the dominating term.

In case of a closed cloud cover, dynamical generation is only about one quarter of that in the broken cloud case. The thermal generation is small but positive at all levels. Thus, both generation mechanisms are acting in this part of the experimental area, but the relative importance of dynamical generation is smaller than farther upstream towards the ice edge.

Observations, e.g., by Brümmer (1985) and Chou and Ferguson (1991), in situations with roll vortices have shown that roll circulations contribute substantially to the total fluxes and variances and that their relative contributions increase with height. Because of the close relationship between roll-scale and subroll-scale fluxes and variances, we presume that the relative magnitudes of the roll-driving mechanisms in the north and south parts of the experimental area are similar to those in the frequency band $\lambda < 1$ km. The satellite image in Figure 4a shows that street-like cloud patterns are already present over the ice. It is highly probable that these structures are mainly driven by wind shear at the inversion because the surface heat flux over the ice or broken ice is presumably small (Walter and Overland, 1984).

The large entrainment at cloud top in the broken compared to the closed cloud case is also obvious in the variance profiles in Figure 19. The different importance of entrainment in both regions is apparent in the variances of Θ, m and v near z_T. Also, the kinetic energy $1/2\ (u'^2 + v'^2 + w'^2)$ near z_T is about 2–3 times larger in the broken than in the closed cloud case. This indirectly supports the validity of the residual estimates of the entrainment fluxes $(\overline{w'\Theta'})_h$ at the top of the boundary layer from the budget considerations; the fluxes are twice as large in the north part of the experimental area as in the south part.

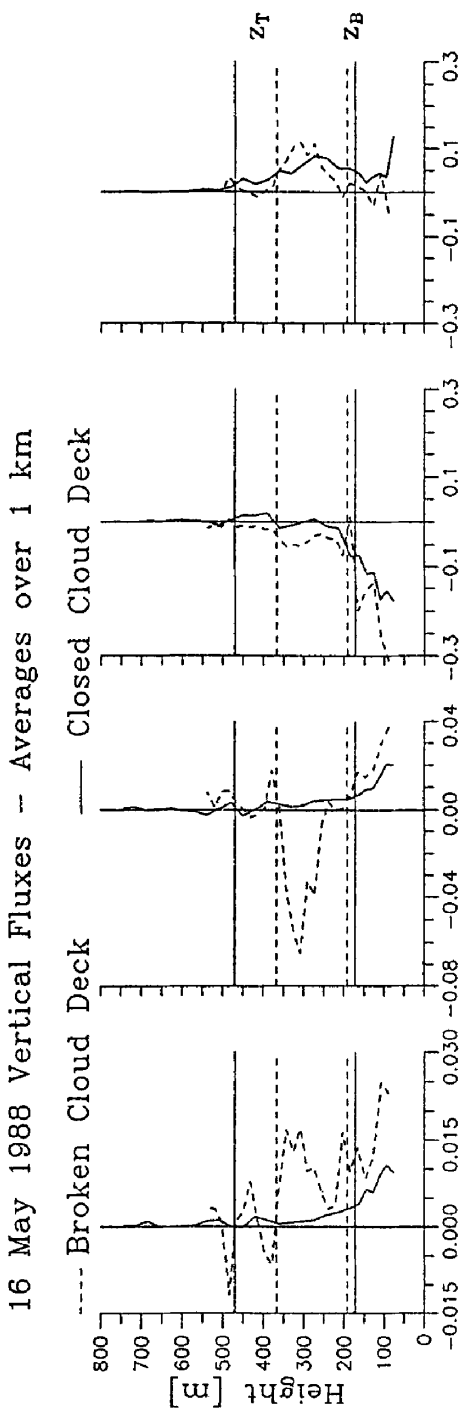

Fig. 17. Vertical fluxes of moisture $w'm'$, potential temperature $w'\Theta'$, alongwind $w'u'$ and crosswind momentum $w'v'$ calculated from 1 km long horizontal subsections of the FALCON profile flights on 16 May 1988. The dashed curves represent averages over the profiles at F1 and F2 with broken clouds and the full curves averages over the profiles at F3 to F6 with a closed cloud deck. The averages are performed relative to cloud base z_B and cloud top z_T so that the characteristic structure is maintained.

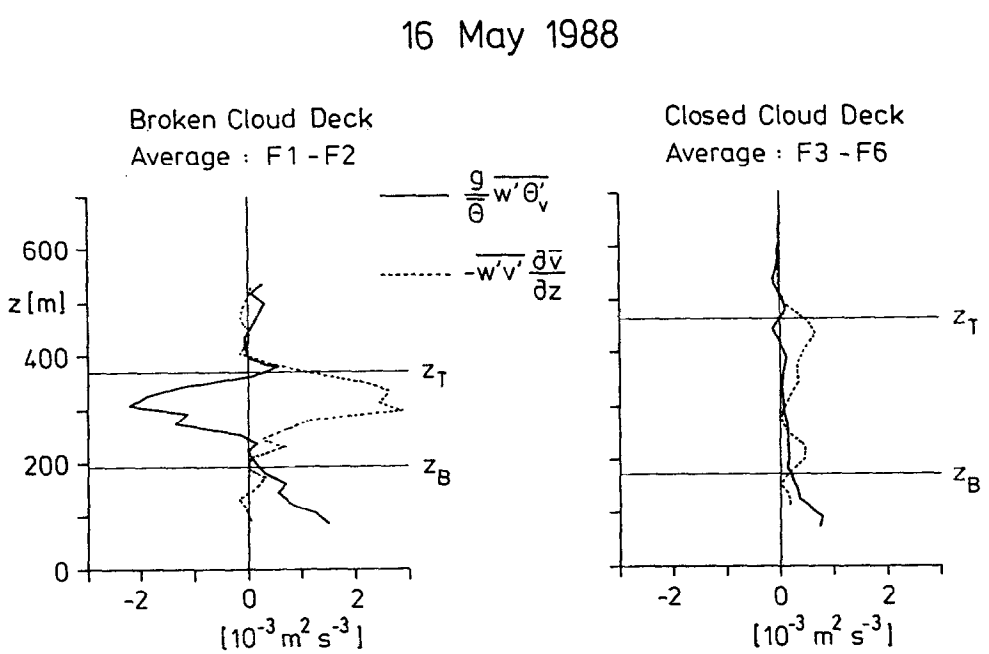

Fig. 18. Vertical profiles of thermal ($g/\Theta\ \overline{w'\Theta_v'}$) and dynamical ($\overline{-w'v'}\ \partial\bar{v}/\partial z$) generation of turbulent kinetic energy in case of a broken (left) and closed cloud deck (right) based on FALCON profile soundings on 16 May 1988.

5. Concluding Remarks

Cold air outbreaks play an important role in the energy exchange between ocean and atmosphere. Sensible heat fluxes of 50 to several 100 W/m^2 in such weather episodes are clearly above the climatological heat flux of 20 W/m^2 averaged over the entire earth surface or of 15 W/m^2 averaged over the ocean surface. According to Budyko (1978), the Greenland Sea and the Barents Sea are those ocean areas of the earth where the surface sensible heat fluxes are largest averaged over a year. The average values amount to more than 50 W/m^2.

The cooling effect of cold air outbreaks on the ocean depends to a great degree on the cloud amounts. Under summer daytime clear-sky conditions, the ocean receives energy even in a cold air outbreak. The strongest cooling of the water occurs under winter nighttime clear-sky conditions. These times are favourable for new ice to be formed at the ice edge and for convection in the ocean to be triggered.

The observations presented here have shown that the amount of boundary-layer clouds depends – among other parameters – on the moisture content above the inversion. This sensitive dependence was demonstrated by the model simulations of Chlond (1992) and in a recent paper by Hanson (1991) on the cloud coverage in marine stratocumulus cloud situations. That the high degree of moisture above the inversion observed on 16 May 1988 is not a rare event can be concluded from Figure 20. It shows the humidity gradient across inversions at the research vessels

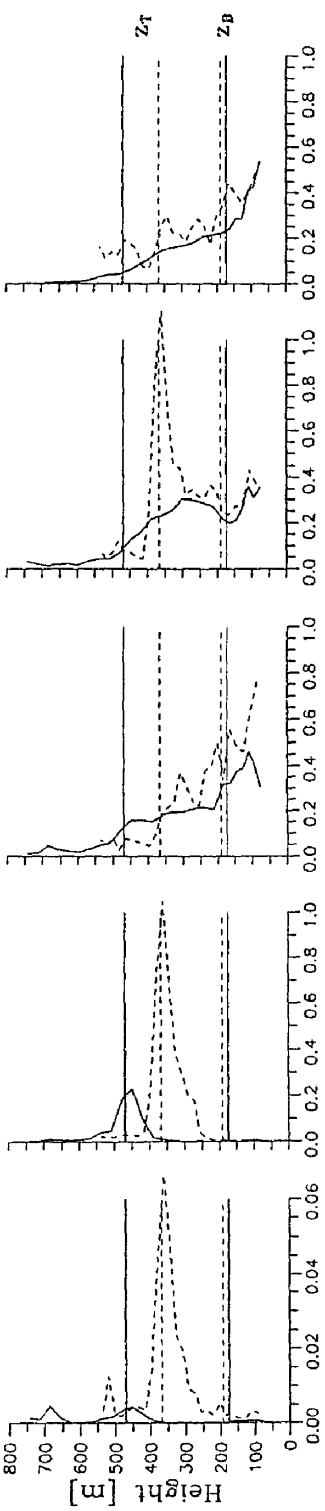

Fig. 19. Variance profiles of water vapour mixing ratio m, potential temperature Θ, alongwind (u), crosswind (v) and vertical (w) wind component. Otherwise as Figure 17.

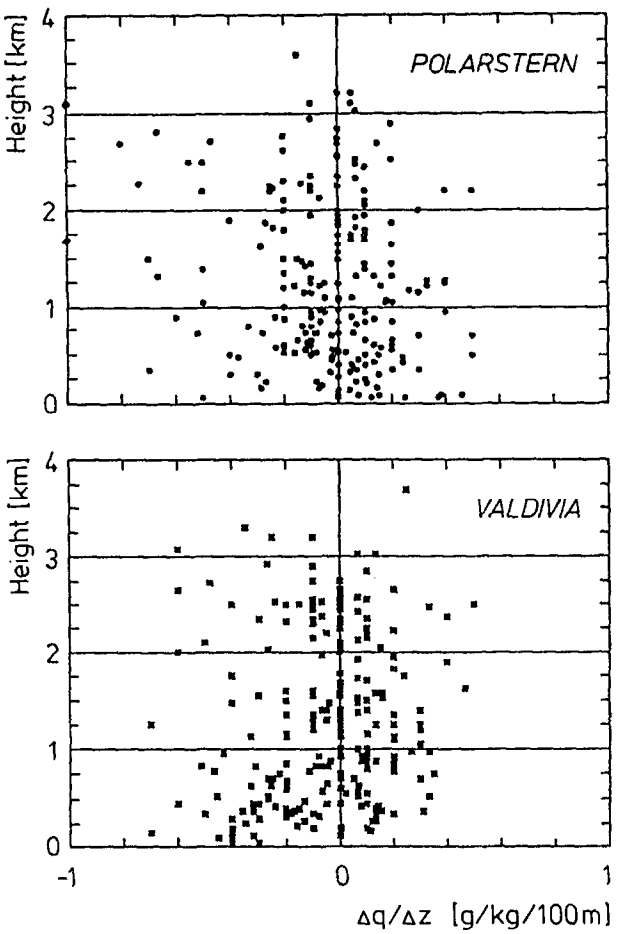

Fig. 20. Vertical gradient of specific humidity $\Delta q/\Delta z$ at low level inversions at the research vessels VALDIVIA and POLARSTERN during the period 5–27 May 1988. The ordinate represents the inversion height. For average location of the ships see Figure 1.

VALDIVIA (in the open water) and POLARSTERN (150 km in the Arctic ice). The figure is based on four-hourly radiosonde ascents during the entire ARKTIS '88 campaign from 5 to 27 May. In nearly one half of the cases, a humidity increase across the inversion was observed.

The cold air outbreak presented here occurs in a relatively shallow layer due to the large-scale anticyclonic weather conditions. In such situations, the entrainment

On 10 May 1988, its magnitude was about two times as large as the sensible heat flux at the surface (Table III) so that H was about $-110\,W/m^2$ in the region with a broken cloud cover and about $-80\,W/m^2$ in the region with a closed cloud deck. On the other hand, the sensible heat flux measurements in Figure 17, which present only the turbulence contribution (scales smaller than 1 km), give values of $-70\,W/m^2$ and $-5\,W/m^2$ in the areas with a broken and closed cloud deck,

respectively. Thus, it may be concluded that a substantial part of the heat flux, namely $-40\,W/m^2$ and $-75\,W/m^2$, is contributed by scales larger than 1 km, presumably mainly by the secondary flow circulations.

References

Atlas, D., Walter, B., and Chou, S.-H.: 1986, 'The Structure of the Unstable Marine Boundary Layer Viewed by Lidar and Aircraft Observations', *J. Atmos. Sci.* **43**, 1301–1318.

Boers, R., Spinhirne, J., and Hart, W., 1988, 'Lidar Observations of the Fine-Scale Structure of Marine Stratocumulus Clouds', *J. Appl. Met.* **27**, 797–810.

Brümmer, B.: 1985, 'Structure, Dynamics and Energetics of Boundary Layer Rolls from KonTur Aircraft Observations', *Contr. Atmosph. Phys.* **58**, 237–254.

Brümmer, B. (ed.): 1989, 'ARKTIS 1988 – Field Phase Report', *Hamb. Geophys. Einzelschriften*, Reihe B, Heft 6.

Budyko, M. I.: 1978, 'The Heat Balance of the Earth', in: J. Gribbin (ed.), *Climatic Change*, Cambridge: Cambridge University Press, pp. 85–113.

Chlond, A.: 1992, 'Three-Dimensional Simulation of Cloud Street Development in a Cold Air Outbreak', *Boundary-Layer Meteorol.* **58**, 161–200.

Chou, S.-H. and Ferguson, M.: 1991, 'Heat Fluxes and Roll Circulations over the Western Gulf Stream during an Intense Cold-Air Outbreak', *Boundary-Layer Meteorol.* **55**, 255–281.

Hanson, H. P.: 1991, 'Cloud Albedo Control by Cloud-Top Entrainment', *Tellus* **43A**, 37–48.

Hein, P. F. and Brown, R. A.: 1988, 'Observations of Longitudinal Roll Vortices during Arctic Cold Air Outbreaks over the Open Water', *Boundary-Layer Meteorol.* **45**, 177–199.

Kelly, R. D.: 1984, 'Horizontal Roll and Boundary Layer Interrelationships Observed over Lake Michigan', *J. Atmos. Sci.* **41**, 1816–1926.

LeMone, M. A.: 1973, 'The Structure and Dynamics of Horizontal Roll Vortices in the Planetary Boundary Layer', *J. Atmos. Sci.* **30**, 1077–1091.

Miura, Y.: 1986, 'Aspect Ratios of Longitudinal Rolls and Convection Cells Observed during Cold Air Outbreaks', *J. Atmos. Sci.* **43**, 26–39.

Walter, B. and Overland, J. E.: 1984, 'Observations of Longitudinal Rolls in a Near Neutral Atmosphere', *Mon. Wea. Rev.* **112**, 200–208.